COMMUNICATION

Check for updates

Novel scalable aerosol-assisted CVD route for perovskite solar cells†‡

S. R. Ratnasingham,[ab] L. Mohan,[ab] M. Daboczi, [ID][c] T. Degousée,[b] R. Binions,§[b] O. Fenwick, [ID][b] J.-S. Kim, [ID][c] M. A. McLachlan [ID][a] and J. Briscoe [ID]*[b]

Organo-metal halide perovskite research has progressed rapidly, with photovoltaic (PV) devices achieving over 25% power conversion efficiency (PCE). However, scalable production of these devices is an ongoing challenge. We demonstrate the growth of methylammonium lead triiodide (MAPI) films *via* a novel two-step aerosol-assisted chemical vapour deposition (AACVD) method leading to the first ever perovskite-based PV devices using active layers deposited by AACVD. This is a scalable deposition process, requiring less complex equipment than conventional CVD. Furthermore, our method utilises methanol (MeOH) as the only solvent, as opposed to harmful solvents typically used in perovskite processing. Structural and optical characterization confirms successful formation of MAPI with no secondary phases and an optical bandgap of ~1.58 eV. The final film had large grains (order of μm), with thickness ranging from 500–1100 nm. These films were used to fabricate working PV devices resulting in a champion PCE of 5.4%. While films demonstrated high structural and compositonal quality, we identified large film roughness as a limiting factor in device PCE, and elucidate the origin of this *via* detailed study of the film growth, which reveals a unique multi-step film formation process.

Introduction

Organo-metal halide perovskite solar cells (PSCs) are one of the most promising PV technologies in development, with large gains in PCE demonstrated over a relatively short period of time. Currently the record PCE for a single junction device is 25.5%,[1] making PSCs competitive with incumbent Si based technologies. The extraordinary performance of these materials can be attributed to several intrinsic material properties such as their broad optical absorption range,[2] long charge carrier diffusion lengths[3] and low exciton binding energies.[4] Furthermore, there are several processing advantages such as a highly-tuneable band gap achieved *via* compositional variation,[5] high defect tolerance due to shallow trap states,[6] versatile processing routes and low cost.[7] The most studied organo-metal halide perovskite is MAPI, in which Pb^{2+} occupies the centre of the octahedra coordinated by six I^- and the A site is occupied by methylammonium ($CH_3NH_3^+$). MAPI has a sharp absorption onset at 800 nm, with a bandgap of approximately 1.58 eV and as of now the highest device PCE exceeds 20%.[8] MAPI has been used in several different architectures, with designs ranging from mesoscopic layouts to planar thin films, with numerous processing routes explored to date.[8] However, a large emphasis still exists on the use of spin coating, as it can be readily optimised to produce high-performance devices. Due to the limited scalability of this process resulting devices tend to have small active areas. This means that large-area deposition methods must be developed to allow for large-scale production of these devices.

Many alternative deposition techniques have been implemented to address the issue of scalability. CVD based techniques are a potential avenue for scalable organo-metal halide perovskite deposition, with several studies fabricating functioning cells using different subtypes of CVD, such as low pressure (LPCVD) and atmospheric pressure (APCVD).[9,10] Whilst scalable, these techniques have certain drawbacks. In LPCVD the low-pressure requirement increases the complexity of the equipment and, therefore, large scale fabrication will incur large capital costs. APCVD negates the need for a low-pressure system, however, it relies on heating precursors above their vaporisation temperature. This is problematic as precursors for halide perovskites tend to be thermally unstable.

AACVD is a promising low-cost alternative to these complex methods. In AACVD, precursors are dissolved in a solvent and

[a] *Department of Materials and Centre for Processable Electronics, Imperial College London, W12 0BZ, UK*

[b] *School of Engineering and Materials Science and Materials Research Institute, Queen Mary University of London, E1 4NS, UK. E-mail: j.briscoe@qmul.ac.uk*

[c] *Department of Physics and Centre for Processable Electronics, Imperial College London, SW7 2AZ, UK*

† We dedicate this paper to Dr Russell Binions, who was supervising Sinclair and Lokeshwari. They were both beginning their academic and scientific journeys when Russel's life was tragically cut short. He was an incredible scientist, musician, supervisor, and friend who is dearly missed.

‡ Electronic supplementary information (ESI) available. See DOI: 10.1039/d0ma00906g

§ Deceased.

delivered as an aerosol into the reactor. This negates concerns over precursor thermal stability. Additionally, the process is conducted at atmospheric pressure making it inexpensive and scalable. Many oxides that are commonly used as electron-transport layers (ETLs) in PSCs have also been deposited by AACVD,[11–13] and we have recently reported deposition of CuSCN *via* AACVD,[14] which has been used as a hole transport layer (HTL) in PSCs.[15] So far, several groups have demonstrated deposition of organo-metal halide perovskites using AACVD, utilising either a 1-step or 2-step method.[16–19] 1-Step deposition generally led to powdery deposits as the precursors tend to homogenously nucleate in the gas phase.[16–19] Previously, we have shown that using a 2-step method overcomes this issue, yielding the first continuous MAPI films using AACVD.[20] However, these films were too thick to form functioning PVs and general film quality was less than ideal as the films contained numerous pinholes. This meant that thus far there have been no working devices prepared using organo-metal halide perovskite absorber layers deposited by AACVD.

In this study, we report the first ever PSCs using an AACVD-deposited active layer. This was achieved *via* a novel 2-step AACVD method, leading to high-quality, pinhole-free MAPI films with thicknesses in the range required to produce functioning PVs. The novel aspects of our method are the use of lead acetate (PbAc$_2$) as the lead source for MAPI, and methanol (MeOH) as the solvent. PbAc$_2$ was first reported as a MAPI precursor by Moore *et al.* and was shown to have favourable crystallisation properties, resulting in high-quality films.[21] Later studies showed solution-processed cells with PCEs exceeding 15%.[22] For AACVD applications, PbAc$_2$ is a novel yet highly suitable precursor as it readily dissolves in many volatile solvents. In our method we use PbAc$_2$ dissolved in MeOH, which is a solvent extensively used in other AACVD systems[23,24] and allows for easy aerosolization due to its low surface tension. The improved reaction conditions within the reactor resulting from the improved aerosol allows better thickness and film quality control, which was a key factor in the realisation of working cells. Importantly, this method provides a route to manufacture organo-metal halide perovskites without the need for harmful and toxic solvents, such as dimethylformamide (DMF), N-methyl-2-pyrrolidone (NMP), gamma butyrolactone (GBL), toluene and chlorobenzene. These solvents are incompatible with large scale ambient processing as they have low exposure limits and would be health hazard to personnel working at manufacturing facilities.[25] Using greener solvents, such as MeOH, can potentially reduce health risks associated with organo-metal halide perovskite processing and make large-scale production more viable.

Results and discussion

SEM analysis of MAPI films deposited by AACVD using our novel 2-step method (see Experimental methods for full details) demonstrates good surface coverage with an average grain size of approximately 1 μm (Fig. 1a). The cross-section in Fig. 1b

Fig. 1 (a) Topographical SEM image of MAPI film deposited *via* AACVD showing large grains. (b) Cross-section SEM image of deposited film, with layers of FTO and mesoporous TiO$_2$ visible. (c) XRD patterns of films deposited *via* AACVD and MAPI reference pattern (ICSD 250735).[31] (d) Tauc plot of AACVD MAPI derived from absorption data. (e) Band diagram of AACVD perovskite material, determined by a combination of UV-Vis, ambient photoemission spectroscopy and Kelvin Probe measurements.

shows a film thickness of approximately 1 μm, with some grains spanning the entire thickness. This morphology is sought after in PV applications, as grain boundaries host defects that act as trap sites for charge carriers, induce shunts and decrease the stability of the cell by allowing the ingress of moisture.[26–29] Furthermore, whilst the films are above the ideal thickness for MAPI-based devices, the lack of grain boundaries should allow charges to be extracted effectively.[30] Also evident from the cross-section is the significant surface roughness, in the order of 100's of nm. This is supported by atomic force microscopy measurements of the surface (Fig S1, ESI‡), which show an R.M.S. roughness of approximately 380 nm. This roughness also gives the films a visual observation of a matte surface, rather than the ideal mirror-smooth finish of spin-coated films.

The XRD patterns of AACVD deposited films show a high degree of phase purity, with no traces of PbAc$_2$ or PbI$_2$ present (Fig. 1c). The XRD pattern of the films match the pattern of a typical tetragonal MAPI thin film, with a preferential orientation around the 110 reflection. Using these data, the lattice parameters were calculated to be 8.83 Å (a) and 12.62 Å (c), which correspond to known literature values.[31] The sharp, narrow peaks indicate a high degree of crystallinity, which is generally desirable in perovskite cells and is typical of MAPI fabricated using an excess of methyl ammonium iodide (MAI).[32] In the AACVD method, the films are exposed to MAI continuously until fully converted to MAPI.

Kelvin probe (KP) and ambient photoemission spectroscopy (APS) measurements (Fig. S4, ESI‡), in conjunction with band gaps derived from absorption measurements, allowed us to construct a band diagram for the MAPI film (Fig. 1e). The Fermi level (E_F) and valence band (E_v) positions were measured to be −4.82 eV and −5.37 eV respectively. Using the bandgap of 1.58 eV obtained from optical absorption (Fig. 1d), places the conduction band at −3.79 eV. The valence band edge values are in excellent agreement with literature values of spin-coated MAPI films.[33,34] The closer to mid-band position of E_F indicates a more intrinsic film, where solution-processed samples typically show more p-type behaviour, with E_F lying closer to E_v owing to intrinsic defects.[35,36] However, as these films are thicker than spin coated films, the measured value is less likely to be influenced by the substrate, which has been observed in thinner films.

The PV performance of the films was evaluated in a n–i–p cell configuration (Fig. 2a and b). Due to the surface roughness of the films, thin layers of organic hole transporting materials (HTMs) were found to be unsuitable; using 2,2′,7,7′-tetrakis-[N,N-di(4-methoxyphenyl)amino]-9,9′-spirobifluorene (Spiro-OMeTAD) gave cells with very low efficiencies due to the incomplete coverage on the rough film (Fig. S5 and S6, ESI‡), and thicker layers do not function due to the low hole mobility of Spiro-OMeTAD. To overcome this, a spray-coated layer of CuSCN was used. This enabled a thicker layer to be deposited to accommodate the roughness, while still allowing charge extraction due to its high hole mobility.[37] Spray-coating is also a scalable deposition method and therefore is complementary to AACVD. Improved PV performance may be achievable by further optimisation of the CuSCN layer thickness, as here the focus was to produce CuSCN layers that were sufficiently thick to fill and cover the rough surface of the perovskite layer.

Statistical distribution of performance parameters for 12 devices and the J–V curve of the champion cell can be seen in Fig. 2c–e. This device had a short circuit current density (J_{sc}) of 16.01 mA cm^{-2}, open circuit voltage (V_{oc}) of 0.77 V, and a fill factor (FF) of 0.44 resulting in a PCE of 5.42%. These results are taken from the reverse scan, with the forward scan having much lower values owing to hysteresis. Although hysteresis is usually observed in this cell architecture, it is very severe in our devices, indicative of non-ideal interfaces. The J_{sc} of the device is lower than the state-of-the-art, which typically exceeds 20 mA cm^{-2}. This loss may originate from both a thicker than
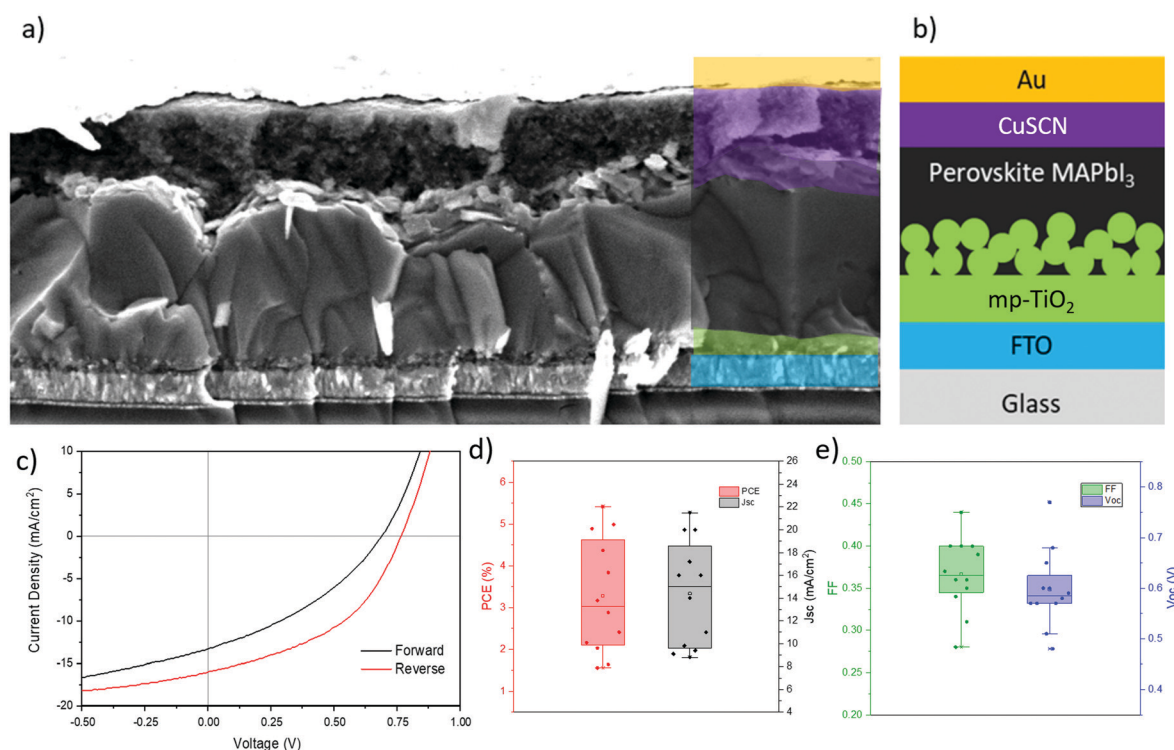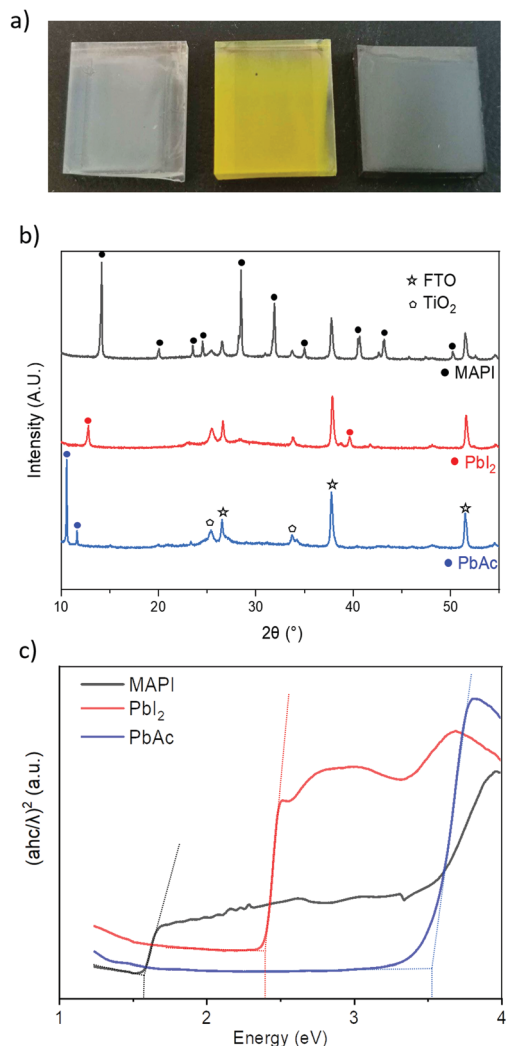

Fig. 2 (a) SEM of completed device cross-section. (b) Schematic of the device configuration used, corresponding to (a). (c) J–V Scan of champion cell showing forward and reverse scans. (d and e) Box-plots of PCE and J_{sc} (d) and FF and V_{oc} (e) of 12 cells, data taken from reverse scans.

Fig. 3 (a) Photographs of three films removed at different stages of the AACVD deposition (substrate size 12 mm × 12 mm). Left: Film after first step. Centre: Film halfway through MAI aerosol exposure. Right: Completed MAPI film (b) XRD patterns correspond to initial $PbAc_2$ film, PbI_2 intermediary and final MAPI film (c) Tauc plots of the three films calculated from absorption data.

ideal perovskite layer (1 μm) and the relatively thick CuSCN layer, both leading to charge collection losses. The low V_{oc} can also be attributed to the non-ideal interface between the rough perovskite and the CuSCN. The cell also suffers from a low FF, induced by both a high series resistance of $\sim 20\ \Omega$ and low shunt resistance of 129 Ω. Again, the high series resistance could be ascribed to the excessive thicknesses of the layers and the shunt resistance could be linked to non-ideal interfaces and pinholes.

To investigate the poor device performance, and to better understand the film formation process, films were characterised at various stages of the deposition (Fig. 3). In the first step a white translucent film of $PbAc_2$ is deposited (Fig. 3a) that upon exposure to the MAI aerosol turns yellow (indicative of PbI_2 formation), on further exposure to MAI a dark film, characteristic of MAPI is formed.
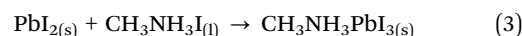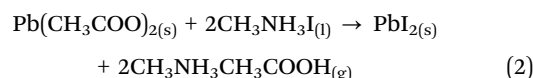
XRD analysis (Fig. 3b) of the initial white film confirmed the presence of $PbAc_2$, while analysis of the yellow film confirmed

that conversion to PbI_2 had occurred. The absence of any $PbAc_2$ in the intermediate film suggests that complete conversion of the acetate to the iodide species occurs before the final conversion to MAPI. This is in contrast to the film formation mechanism in solution-processed films using $PbAc_2$ as the lead source, where typically no intermediate phases form.[38] UV-Vis absorption measurements seen in Fig. 3c further support the proposed film formation mechanism, with absorption onset and bandgap values matching literature values of $PbAc_2$, PbI_2 and MAPI (3.5 eV, 2.3 eV and 1.55 eV).[39]

Eqn (1) shows the typically reported MAPI formation scheme when using $PbAc_2$ as the Pb(II) source.[38]

$$Pb(CH_3COO)_{2(s)} + 3CH_3NH_3I_{(l)} \rightarrow CH_3NH_3PbI_{3(s)}$$
$$+ 2CH_3NH_3CH_3COO_{(g)} \qquad (1)$$
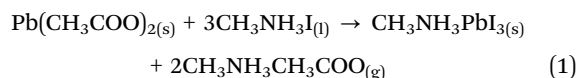
In this process the $PbAc_2$ reacts with the MAI to form MAPI and $CH_3NH_3CH_3COO$ (MAAc), which is removed via the annealing process. From our observations of the AACVD deposition we propose a two-step scheme, summarised in eqn (2) and (3).

$$Pb(CH_3COO)_{2(s)} + 2CH_3NH_3I_{(l)} \rightarrow PbI_{2(s)}$$
$$+ 2CH_3NH_3CH_3COOH_{(g)} \qquad (2)$$

$$PbI_{2(s)} + CH_3NH_3I_{(l)} \rightarrow CH_3NH_3PbI_{3(s)} \qquad (3)$$

In the first step $PbAc_2$ is transformed to PbI_2, and the volatile species MAAc is formed. We anticipate that the MAAc will exist in equilibrium with CH_3NH_2 and acetic acid, both of which are highly volatile and will be driven off under the reaction conditions (220 °C). The second process is akin to a typical solution process and involves the reaction of PbI_2 with MAI, leading to the formation of MAPI.

This film formation mechanism could explain the origin of the surface roughness observed in the final film. Large density changes during film formation, beginning from 3.25 g cm^{-3} ($PbAc_2$)[40] to 6.16 g cm^{-3} (PbI_2)[41] and then finally to 4 g cm^{-3} (MAPI),[42] would cause the films to contract and swell. This would lead to an uneven film with a rough surface. Moreover, work by Brenner et al. explored vapour phase transformation of PbI_2 single crystals exposed to gaseous MAI.[43] Like our work, the transformation of the films was accompanied by a roughening of the surface, likely attributed to the expansion and growth of the MAPI grains. Further work will be needed to find a suitable set of precursors that may minimize the density change, and therefore improve final film quality. Going forward, this method could be used to grow other organo-metal halide perovskites which exhibit better optoelectronic properties, such as formamidinium-based, or mixed cation perovskites.[44] These compositions may allow for the thicker films deposited via this method to perform better, due to their longer diffusion lengths.

Conclusion

We have successfully demonstrated the use of a novel AACVD method to fabricate operational MAPI PVs. The method relies on the use of green solvents, potentially making it a safer

route for large scale deposition of perovskites. The resulting champion device had a PCE of 5.4%, and whilst this is low compared to the state-of-the-art perovskite devices, it is the highest PCE recorded for any PV device utilising an AACVD active layer.[45] Furthermore, we show evidence of a unique multi-step film formation process, with the films forming a PbI$_2$ intermediate phase before converting to MAPI. Overall, we have demonstrated that exploring wider precursor-solvent systems is a promising route to successfully fabricate PSCs via AACVD, and that identification of further systems that do not undergo such dramatic density changes may be the key to achieving high PCEs via AACVD.

Experimental methods

10 mm × 10 mm fluorine-doped tin oxide (FTO) coated glass substrates were patterned and etched using 1 M HCl and zinc powder. The substrates were then cleaned with detergent, acetone and isopropanol using an ultrasonic bath, before undergoing UV-ozone treatment. A layer of compact TiO$_2$ was spin-coated using a 0.2 mol dm^{-3} titanium isopropoxide solution in ethanol, with the addition of 0.02 mol dm^{-3} HCl, at 5000 rpm. This was dried for 10 minutes at 120 °C. Mesoporous TiO$_2$ was then deposited using a solution of 18-NRT titania paste (Sigma) diluted in ethanol (1 : 7 wt%), which was spin-coated at 5000 rpm. The substrates were then annealed at 500 °C for 1 hour.

MAPI was deposited on top of the ETL-covered substrates via a sequential 2-step deposition method. The substrates were treated by UV-ozone before being placed into a cold wall AACVD reactor. The maximum deposition area of the reactor is 14 cm × 7 cm, with up to six, 12 mm × 12 mm substrates being placed in the centre of the reactor where the deposition is most homogenous. The inhomogeneity arises from aerodynamic effects within the reactor as the deposition area is close to the reactor walls. Larger reactors designed with more optimised geometries would allow for much larger deposition areas. Fig. S2 (ESI‡) shows the largest substrate dimensions we were able to deposit homogeneously. The first-step precursor solution was formed of a 0.13 mol dm^{-3} solution of lead(II) acetate trihydrate (Aldrich) in anhydrous MeOH. The solution was then aerosolised using an ultrasonic mister and flowed into the reactor via a nitrogen gas flow. The gas flow was monitored using a flow meter and set to 0.5 dm^{-3} min^{-1}. The substrate was heated to 175 °C before the deposition commenced. This first step was completed in 30 minutes, with the substrate kept at 175 °C. The second precursor was a 0.21 mol dm^{-3} solution of methyl ammonium iodide in anhydrous MeOH. The substrate temperature was increased from 175 °C to 220 °C before the second precursor was delivered at 0.3 dm^{-3} min^{-1}. This step was completed in 60 minutes. The substrate was then cooled before being placed into a desiccator to eliminate sources of moisture. A schematic of the experimental setup can be seen in Fig. S3 (ESI‡).

The CuSCN HTM was deposited using a 0.15 mol dm^{-3} solution of CuSCN (Aldrich) in dipropyl sulphide using a

method adapted from a previous study.[46] The substrates were heated to 65 °C and 30 spray passes were used. This forms an approximately 300 nm thick layer of CuSCN. The substrates were then stored in a glovebox for one day to allow the layer to dry. The Spiro-OMeTAD solution was made by dissolving in chlorobenzene to form a 70 mmol dm^{-3} solution. This solution was then doped using a 4-tert-butylpyridine (TBP) and bis(trifluoromethane)-sulfonimide lithium salt (Li-TFSI). Per ml of Spiro-OMeTAD solution, 30 μl of TBP were added. This was followed by 20 μl of 1.8 mol dm^{-3} Li-TFSI in acetonitrile. The doped solution was then spin coated on the AACVD MAPI at 3000 rpm for 30 s. Samples were then aged for 24 hours in a desiccator to allow for the oxidation of spiro-OMeTAD. The cell was completed by thermally evaporating 100 nm of Au through a shadow mask to form the top contacts, which defined the cell area as 0.45 cm^2.

The morphology of the MAPI films was measured using a FEI Inspect-F field emission scanning electron microscope. Cross-sections were taken by cleaving cell substrates. All images were taken at a 5 kV accelerating voltage to avoid damage or alter the morphology of the film. The MAPI crystal structure was investigated using a Panalytical X'Pert Powder X-Ray Diffractometer, set up in the Bragg–Brentano geometry using CuKα (λ = 1.541 Å) radiation. Optical absorption measurements were taken utilising a Shimadzu UV-2600 spectrophotometer with an integrating sphere attachment in a wavelength range of 300–1000 nm.

Film topography was recorded by atomic force microscopy (AFM) in semi-contact mode, using a Ntegra Prima (NT-MDT Spectrum Instruments) mounted on an TS-150 isolation table (Table Stable Ltd). Pyramidal silicon etched AFM probes (tip radius of 8 nm, Agar Scientific) were used for the measurements. Images of 40 × 40 μm (256 lines) were recorded at 0.5 Hz line rate. The tip set-point was adjusted between samples to minimize the feedback noise. Once recorded, the images of the films were corrected with Gwyddion to extract the film R.M.S. roughness.

The energy level measurements were performed using an APS04 System (KP Technology). The Fermi level of the samples was determined in dark by Kelvin probe (KP) applying a vibrating gold tip (2 mm diameter). A cleaned silver reference was used to calibrate the work function of the tip. The samples were deposited on a conductive substrate, grounded during the measurement, and kept in dark until an equilibrium value was reached. Ambient photoemission spectroscopy (APS) measurements were performed to determine the valence band edge of the semiconductor layer. The cube root of the photoemission signal was fitted with a linear and extrapolated to zero to extract the energy value of the valence band edge.

Device J–V curves were measured using a Keithley 2400 Source meter scanning at 0.03 V s^{-1}. To measure the light response, devices were placed under simulated AM 1.5G solar light irradiation from a Newport class ABB solar simulator, calibrated to 1 Sun (100 mA cm^{-2}) using a Si reference cell (Newport). Devices were light soaked for 30 s prior to starting the J–V scan.

Conflicts of interest

There are no conflicts to declare.

Acknowledgements

Notes and references

1 Best Research-Cell Efficiency Chart | Photovoltaic Research | NREL.

2 Q. Lin, A. Armin, R. C. R. Nagiri, P. L. Burn and P. Meredith, Electro-Optics of Perovskite Solar Cells, *Nat. Photonics*, 2015, **9**, 106–112.

3 L. M. Charge-Carrier Herz, Mobilities in Metal Halide Perovskites: Fundamental Mechanisms and Limits, *ACS Energy Lett.*, 2017, **2**, 1539–1548.

4 A. Miyata, A. Mitioglu, P. Plochocka, O. Portugall, J. T. W. Wang, S. D. Stranks, H. J. Snaith and R. J. Nicholas, Direct Measurement of the Exciton Binding Energy and Effective Masses for Charge Carriers in Organic–Inorganic Tri-Halide Perovskites, *Nat. Phys.*, 2015, **11**, 582–587.

5 D. P. McMeekin, G. Sadoughi, W. Rehman, G. E. Eperon, M. Saliba, M. T. Hörantner, A. Haghighirad, N. Sakai, L. Korte and B. Rech, *et al.*, A Mixed-Cation Lead Mixed-Halide Perovskite Absorber for Tandem Solar Cells, *Science*, 2016, **351**, 151–155.

6 M. Yavari, F. Ebadi, S. Meloni, Z. S. Wang, T. C.-J. Yang, S. Sun, H. Schwartz, Z. Wang, B. Niesen and J. Durantini, *et al.*, How Far Does the Defect Tolerance of Lead-Halide Perovskites Range? The Example of Bi Impurities Introducing Efficient Recombination Centers, *J. Mater. Chem. A*, 2019, **7**(41), 23838–23853.

7 T. P. Osedach, T. L. Andrew and V. Bulović, Effect of Synthetic Accessibility on the Commercial Viability of Organic Photovoltaics, *Energy Environ. Sci.*, 2013, **6**, 711–718.

8 S. Akin, N. Arora, S. M. Zakeeruddin, M. Grätzel, R. H. Friend and M. I. Dar, New Strategies for Defect Passivation in High-Efficiency Perovskite Solar Cells, *Adv. Energy Mater.*, 2020, **10**, 1–29.

9 A. K. Jena, A. Kulkarni and T. Miyasaka, Halide Perovskite Photovoltaics: Background, Status, and Future Prospects, *Chem. Rev.*, 2019, **119**, 3036–3103.

10 P. S. Shen, J. S. Chen, Y. H. Chiang, M. H. Li, T. F. Guo and P. Chen, Low-Pressure Hybrid Chemical Vapor Growth for Efficient Perovskite Solar Cells and Large-Area Module, *Adv. Mater. Interfaces*, 2016, **3**, 8.

11 P. Luo, Z. Liu, W. Xia, C. Yuan, J. Cheng and Y. Lu, Uniform, Stable, and Efficient Planar-Heterojunction Perovskite Solar Cells by Facile Low-Pressure Chemical Vapor Deposition under Fully Open-Air Conditions, *ACS Appl. Mater. Interfaces*, 2015, **7**(4), 2708–2714.

12 M. J. Powell, D. B. Potter, R. L. Wilson, J. A. Darr, I. P. Parkin and C. J. Carmalt, Scaling Aerosol Assisted Chemical Vapour Deposition: Exploring the Relationship between Growth Rate and Film Properties, *Mater. Des.*, 2017, **5**, 116–124.

13 P. Marchand, I. A. Hassan, I. P. Parkin and C. J. Carmalt, Aerosol-Assisted Delivery of Precursors for Chemical Vapour Deposition: Expanding the Scope of CVD for Materials Fabrication, *Dalton Trans.*, 2013, **42**, 9406–9422.

14 N. Noor and I. P. Parkin, Enhanced Transparent-Conducting Fluorine-Doped Tin Oxide Films Formed by Aerosol-Assisted Chemical Vapour Deposition, *J. Mater. Chem. C*, 2013, **1**, 984–996.

15 L. Mohan, S. R. Ratnasingham, J. Panidi, T. D. Anthopoulos, R. Binions, M. A. McLachlan and J. Briscoe, Low Temperature Scalable Deposition of Copper(I) Thiocyanate Films via Aerosol-Assisted Chemical Vapor Deposition, *Cryst. Growth Des.*, 2020, 5380–5386.

16 N. Arora, M. I. Dar, A. Hinderhofer, N. Pellet, F. Schreiber, S. M. Zakeeruddin and M. Grätzel, Perovskite Solar Cells with CuSCN Hole Extraction Layers Yield Stabilized Efficiencies Greater than 20%, *Science*, 2017, **358**, 768–771.

17 D. S. Bhachu, D. O. Scanlon, E. J. Saban, H. Bronstein, I. P. Parkin, C. J. Carmalt and R. G. Palgrave, Scalable Route to $CH_3NH_3PbI_3$ Perovskite Thin Films by Aerosol Assisted Chemical Vapour Deposition, *J. Mater. Chem. A*, 2015, **3**, 9071–9073.

18 M. Afzaal, B. Salhi, A. Al-Ahmed, H. M. Yates and A. S. Hakeem, Surface-Related Properties of Perovskite $CH_3NH_3PbI_3$ Thin Films by Aerosol-Assisted Chemical Vapour Deposition, *J. Mater. Chem. C*, 2017, 8366–8370.

19 J. C. Ke, D. J. Lewis, A. S. Walton, B. F. Spencer, P. O'Brien, A. G. Thomas and W. R. Flavell, Ambient-Air-Stable Inorganic Cs_2SnI_6 Double Perovskite Thin Films via Aerosol-Assisted Chemical Vapour Deposition, *J. Mater. Chem. A*, 2018, **6**, 11205–11214.

20 D. J. Lewis and P. O'Brien, Ambient Pressure Aerosol-Assisted Chemical Vapour Deposition of $(CH_3NH_3)PbBr_3$, an Inorganic-Organic Perovskite Important in Photovoltaics, *Chem. Commun.*, 2014, **50**, 6319–6321.

21 S. Chen, J. Briscoe, Y. Shi, K. Chen, R. M. Wilson, S. Dunn and R. Binions, A Simple, Low-Cost CVD Route to High-Quality $CH_3NH_3PbI_3$ Perovskite Thin Films, *CrystEngComm*, 2015, **17**, 7486–7489.

22 D. T. Moore, H. Sai, K. W. Tan, D. M. Smilgies, W. Zhang, H. J. Snaith, U. Wiesner and L. A. Estroff, Crystallization Kinetics of Organic-Inorganic Trihalide Perovskites and the Role of the Lead Anion in Crystal Growth, *J. Am. Chem. Soc.*, 2015, **137**, 2350–2358.

23 W. Zhang, M. Saliba, D. T. Moore, S. K. Pathak, M. T. Hörantner, T. Stergiopoulos, S. D. Stranks, G. E. Eperon, J. A. Alexander-Webber and A. Abate, *et al.*, Ultrasmooth Organic–Inorganic Perovskite Thin-Film Formation and Crystallization for Efficient Planar Heterojunction Solar Cells, *Nat. Commun.*, 2015, **6**, 6142.

24 C. E. Knapp and C. J. Carmalt, Solution Based CVD of Main Group Materials, *Chem. Soc. Rev.*, 2016, **45**, 1036–1064.

25 C. Edusi, G. Hyett, G. Sankar and I. P. Parkin, Aerosol-Assisted CVD of Titanium Dioxide Thin Films from Methanolic Solutions of Titanium Tetraisopropoxide; Substrate

and Aerosol-Selective Deposition of Rutile or Anatase, *Chem. Vap. Deposition*, 2011, **17**, 30–36.

26 S. M. Jain, T. Edvinsson and J. R. Durrant, Green Fabrication of Stable Lead-Free Bismuth Based Perovskite Solar Cells Using a Non-Toxic Solvent, *Chem. Commun.*, 2019, **2**, 91.

27 J. M. Ball and A. Petrozza, Defects in Perovskite-Halides and Their Effects in Solar Cells, *Nat. Energy*, 2016, 1.

28 W. J. Yin, T. Shi and Y. Yan, Unusual Defect Physics in $CH_3NH_3PbI_3$ Perovskite Solar Cell Absorber, *Appl. Phys. Lett.*, 2014, 104.

29 Y. Shao, Y. Fang, T. Li, Q. Wang, Q. Dong, Y. Deng, Y. Yuan, H. Wei, M. Wang and A. Gruverman, *et al.*, Grain Boundary Dominated Ion Migration in Polycrystalline Organic–Inorganic Halide Perovskite Films, *Energy Environ. Sci.*, 2016, **9**, 1752–1759.

30 N. Aristidou, C. Eames, I. Sanchez-Molina, X. Bu, J. Kosco, M. Saiful Islam and S. A. Haque, Fast Oxygen Diffusion and Iodide Defects Mediate Oxygen-Induced Degradation of Perovskite Solar Cells, *Nat. Commun.*, 2017, **8**, 15218.

31 Z. Chu, M. Yang, P. Schulz, D. Wu, X. Ma, E. Seifert, L. Sun, X. Li, K. Zhu and K. Lai, Impact of Grain Boundaries on Efficiency and Stability of Organic–Inorganic Trihalide Perovskites, *Nat. Commun.*, 2017, 2230.

32 C. C. Stoumpos, C. D. Malliakas and M. G. Kanatzidis, Semiconducting Tin and Lead Iodide Perovskites with Organic Cations: Phase Transitions, High Mobilities, and near-Infrared Photoluminescent Properties, *Inorg. Chem.*, 2013, **52**, 9019–9038.

33 T. Du, J. Kim, J. Ngiam, S. Xu, P. R. F. Barnes, J. R. Durrant and M. A. McLachlan, Elucidating the Origins of Subgap Tail States and Open-Circuit Voltage in Methylammonium Lead Triiodide Perovskite Solar Cells, *Adv. Funct. Mater.*, 2018, **28**, 1801808.

34 T. Du, W. Xu, M. Daboczi, J. Kim, S. Xu, C. T. Lin, H. Kang, K. Lee, M. J. Heeney and J. S. Kim, *et al.*, P-Doping of Organic Hole Transport Layers in p–i–n Perovskite Solar Cells: Correlating Open-Circuit Voltage and Photoluminescence Quenching, *J. Mater. Chem. A*, 2019, **7**, 18971–18979.

35 M. Daboczi, J. S. Kim, J. Lee, H. Kang, I. Hamilton, C. T. Lin, S. D. Dimitrov, M. A. McLachlan, K. Lee and J. R. Durrant, *et al.*, Towards Efficient Integrated Perovskite/Organic Bulk Heterojunction Solar Cells: Interfacial Energetic Requirement to Reduce Charge Carrier Recombination Losses, *Adv. Funct. Mater.*, 2020, **2001482**, 1–8.

36 L. A. Frolova, N. N. Dremova and P. A. Troshin, The Chemical Origin of the P-Type and n-Type Doping Effects in the Hybrid Methylammonium–Lead Iodide ($MAPbI_3$) Perovskite Solar Cells, *Chem. Commun.*, 2015, **51**, 14917–14920.

37 M. Daboczi, I. Hamilton, S. Xu, J. Luke, S. Limbu, J. Lee, M. A. McLachlan, K. Lee, J. R. Durrant and I. D. Baikie, *et al.*, Origin of Open-Circuit Voltage Losses in Perovskite Solar Cells Investigated by Surface Photovoltage Measurement, *ACS Appl. Mater. Interfaces*, 2019, **11**, 46808–46817.

38 N. Wijeyasinghe, A. Regoutz, F. Eisner, T. Du, L. Tsetseris, Y. H. Lin, H. Faber, P. Pattanasattayavong, J. Li and F. Yan, *et al.*, Copper(ı) Thiocyanate (CuSCN) Hole-Transport Layers Processed from Aqueous Precursor Solutions and Their Application in Thin-Film Transistors and Highly Efficient Organic and Organometal Halide Perovskite Solar Cells, *Adv. Funct. Mater.*, 2017, **27**, 1–13.

39 Y. Chen, A. S. Yerramilli, L. Li, W. Qu, Y. Shen, Y. Song and T. L. Alford, Control of the Nucleation and Growth of the Lead Acetate Solution Derived $CH_3NH_3PbI_3$ Films Leads to Enhanced Power Conversion Efficiency, *ACS Appl. Energy Mater.*, 2018, **1**, 2898–2906.

40 R. Ahuja, H. Arwin, A. F. Da Silva, C. Persson, J. M. Osorio-Guillén, J. Souza De Almeida, C. M. Araujo, E. Veje, N. Veissid and C. Y. An, *et al.*, Electronic and Optical Properties of Lead Iodide, *J. Appl. Phys.*, 2002, **92**, 7219–7224.

41 National Center for Biotechnology Information. PubChem Database. Lead(ii) acetate, CID = 9317, Lead iodide | PbI2 - PubChem.

42 M. Stuckelberger, T. Nietzold, G. N. Hall, B. West, J. Werner, B. Niesen, C. Ballif, V. Rose, D. P. Fenning and M. I. Bertoni, Charge Collection in Hybrid Perovskite Solar Cells: Relation to the Nanoscale Elemental Distribution, *IEEE J. Photovoltaics*, 2017, 590–597.

43 T. M. Brenner, Y. Rakita, Y. Orr, E. Klein, I. Feldman, M. Elbaum, D. Cahen and G. Hodes, Conversion of Single Crystalline PbI₂ to $CH_3NH_3PbI_3$: Structural Relations and Transformation Dynamics, *Chem. Mater.*, 2016, **28**, 6501–6510.

44 F. Alam and D. J. Lewis, Thin films of formamidinium lead iodide (FAPI) deposited using aerosol assisted chemical vapour deposition (AACVD), *Sci. Rep.*, 2020, **10**, 1–7.

45 A. F. Hepp, J. S. McNatt, J. E. Dickman, M. H. C. Jin, K. K. Banger, C. V. Kelly, A. R. Aquino Gonzalez and A. A. Rockett, Aerosol-Assisted Chemical Vapor Deposited Thin Films for Space Photovoltaics, *Collect. Tech. Pap. - 4th Int. Energy Convers. Eng. Conf*, 2006, **1**, 100–114.

46 S. M. Hatch, J. Briscoe and S. Dunn, Improved CuSCN–ZnO Diode Performance with Spray Deposited CuSCN, *Thin Solid Films*, 2013, **531**, 404–407.